

RESEARCH

Open Access



Dynamic Properties of Strain-Hardening Cementitious Composite Reinforced with Basalt and Steel Fibers

Na Zhang^{1,2}, Jian Zhou^{1*} and Guo-wei Ma¹

Abstract

Strain-hardening cementitious composites (SHCCs) reinforced with both basalt and steel fibers are expected to possess the advantages of both fiber materials and exhibit desirable mechanical properties. In this study, we experimentally investigated the dynamic mechanical properties of an SHCC reinforced with inorganic fibers of basalt and steel for different strain rates (10^1 to 10^2 s^{-1}) using a 50-mm-diameter Split-Hopkinson pressure bar. The effects of the strain rate on the dynamic compressive strength and dynamic splitting strength as well as the dynamic increase factor and energy absorption characteristics of the SHCC were analyzed. The results showed that all the mechanical indices increased with an increase in the strain rate. The dynamic increase factors of the compressive strength and splitting strength increased linearly with the decimal logarithm of the strain rate. Further, the addition of the basalt and steel fibers resulted in a significant increase in the strain-rate sensitivity of the dynamic mechanical behavior of the SHCC, with the effect of the steel fibers being more pronounced than that of the basalt fibers. Although the basalt and steel fibers had varying effects on the strain-rate sensitivity of the dynamic mechanical behavior of the SHCC based on the fiber content, there were significant positive correlations between the type and content of the fibers used and the strain-rate sensitivity.

Keywords: strain-hardening cementitious composites, basalt fibers, steel fibers, split-Hopkinson pressure bar

1 Introduction

Cementitious materials are inherently brittle and easy to crack and thus exhibit poor mechanical properties and long-term durability problems. For decades, significant efforts have been made to overcome these drawbacks. In the 1990s, based on a comprehensive study of the micromechanics of the interactions between the fibers, matrix, and fiber–matrix interface, Li and Leung (1992) and Maalej and Li (1994) developed a series of ultra ductile fiber-reinforced cementitious materials, which were named engineered cementitious composites (ECCs). Under tensile loads, ECCs show tensile-strain-hardening

behavior and exhibit a tensile strain capacity in the range of 3–7%, which is higher than that of normal concrete and normal fiber-reinforced concrete (FRC) (0.01%). The main difference in the tensile properties of ECCs, normal concrete, and FRC is that, after cracking, ECCs exhibit strain-hardening behavior, which is accompanied by the formation of multiple cracks, whose width remains narrow. In contrast, ordinary concrete exhibits a sudden drop in its load-carrying capacity while FRC exhibits strain softening. As the strain rate is increased, the tensile strength of ECCs increases while their tensile ductility decreases (Yang and Li 2005; Mechtcherine et al. 2011). ECCs are being used in a broad range of applications, including as the link slabs on bridge decks and in the coupling beams in high-rise buildings to enhance their seismic resistance and composite ECC/steel bridge deck as well as for concrete repair.

*Correspondence: zhoujian@hebut.edu.cn

¹ School of Civil and Transportation Engineering, Hebei University of Technology, Tianjin 300401, China

Full list of author information is available at the end of the article

Journal information: ISSN 1976-0485 / eISSN 2234-1315

However, cementitious materials are subjected to not only static loads but also dynamic ones (i.e., those corresponding to earthquakes and air blasts) during their service life. Many researchers have found that ECCs exhibit significantly better impact resistance (Yang et al. 2012; Zhang et al. 2007). Maalejet al. (2005) concluded that ECCs with steel and polyethylene (PE) fibers show higher tensile strength as the strain rate is increased. Soe et al. (2013) also studied the dynamic tensile properties of hybrid fiber ECCs for increasing strain rates (from 10^{-5} to 10^{-1} s $^{-1}$). Compared with an ECC reinforced only with PE fibers, an ECC reinforced with both PE and steel fibers showed higher tensile strength and tensile strain capacity. Moreover, Li et al. (2016) concluded that the addition of steel fibers improves the dynamic behavior of ultrahigh-toughness cementitious composites, even when the volume content of polyvinyl alcohol (PVA) fibers is kept constant at 2%. Ali et al. (2017) performed the drop-weight impact test and found that the dynamic performance of ECCs improves with the addition of PVA and shape memory alloy fibers. The static and dynamic mechanical properties of concrete reinforced with basalt fibers (BFs) and PP fibers have also been studied (Fu et al. 2018; Wang et al. 2019). It was found the combined use of both BFs and PP fibers is effective in enhancing the mechanical properties of concrete.

With the increase in the use of ECCs in the construction of infrastructure- and transportation-related structures, the performance of these materials at elevated temperatures has become a matter of concern, since such structures may experience impacts, blasts, and fires either simultaneously or sequentially, and their combined effects should be taken into account. The high ductility of ECCs results from the bridging behavior of the polymer fibers within the cementitious matrix. However, most current research efforts focus on organic fibers, and these fibers do not have high temperature resistance. For instance, PVA fibers, which are used mostly widely in ECCs, melt at approximately 230 °C. This would cause the ECC to lose its tensile-strain-hardening characteristics (Yu et al. 2015; Bhat et al. 2014).

Basalt fibers are a new type of inorganic fibers with excellent mechanical properties and are being used widely in many fields (Kizilkanat et al. 2015). BFs are continuous fibers obtained by crushing pure natural basalt

ore, melting it at a high temperature (1450–1500 °C), and stretching it through a spinneret. They show superior tensile strength, temperature resistance, and ablation resistance (Jiang et al. 2014; Branston et al. 2016), are cost effective, and can be readily incorporated into cement-based materials (Lopresto et al. 2011; Borhan et al. 2012). Thus, BFs can improve the flexural strength, toughness (Lee et al. 2014), and fracture energy characteristics of cement matrix composites (Sim et al. 2005; Ralegaonkar et al. 2018). Moreover, a recent study has confirmed the feasibility of fabricating ECCs using BFs (Song 2019).

In order to further improve the impact resistance of ECCs, in this study, we propose two-scale fiber reinforcement using BFs and steel fibers (SFs). The BFs, with a diameter of 14 μ m, would bridge small cracks, while the SFs, with a diameter of 200 μ m, would bridge larger cracks. This would help control the fracture process of the cementitious matrix.

Engineered cementitious composites known as strain-hardening cementitious composites (SHCCs) exhibit strain-hardening behavior. This study aimed to investigate the dynamic mechanical properties of an SHCC reinforced with both BFs and SFs at variable strain rates (10^1 to 10^2 s $^{-1}$). The performance of the BF/SF-containing SHCC under compression and a splitting load at different strain rates was studied experimentally, and its energy-absorption characteristics were analyzed systematically. The effects of the two fiber types individually as well as together in various volume fractions on the impact resistance of the SHCC were also elucidated. The results of this study shed light on the effects of reinforcing BFs and SFs on the impact resistance of SHCCs when subjected to high-strain-rate loads.

2 Materials and Methods

2.1 Mixture Compositions

The following cementitious materials were used to prepare the SHCC specimens: aluminate cement, fly ash (class F, type I) corresponding to Chinese standards (GB1596-88 1988), silica fume, water-reducing agent, BFs, SFs, and water. Table 1 lists the chemical compositions and physical properties of the materials, which were produced by local manufacturers in Tianjin.

The physical, mechanical, and surface properties of the fibers are listed in Table 2. The BFs exhibited a tensile

Table 1 Chemical compositions of the materials.

Material	SiO ₂	Al ₂ O ₃	Fe ₂ O ₃	CaO	MgO	SO ₃	LOI
Aluminate cement	7.95	50.33	2.38	32.6	2.03	–	0.57
Fly ash	48.63	37.37	3.78	3.05	1.60	84.00	3.61
Silica fume	87.28	1.09	0.75	0.87	1.76	1.47	4.74

Table 2 Physical and mechanical properties of basalt and steel fibers.

Fiber type	Density (g/cm ³)	Tensile strength (MPa)	Elastic modulus (GPa)	Length (mm)	Diameter (μm)	Elongation (%)
Basalt fibers	2.695	2230	85.8	12	14.1	2.85
Steel fibers	7.86	2200	201	13	200	–

Table 3 Mixture compositions of SHCC specimens.

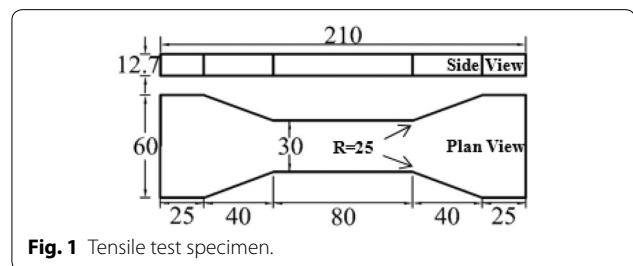
Specimen ID	Binder (100%)			Water-reducing agent (weight%)	Basalt fibers (volume%)	Steel fibers (volume%)	Water/binder (%)
	Aluminate cement (%)	Fly ash (%)	Silica fume (%)				
BF0SF0	40	50	10	0.4	0	0	20
BF2SF1	40	50	10	0.4	2	1	20
BF2.5SF0.5	40	50	10	0.4	2.5	0.5	20
BF3SF0	40	50	10	0.4	3	0	20

strength similar to that of the SFs but had a lower elastic modulus. For comparison, the amount of SFs used in the SHCC was reduced gradually while that of the BFs was increased commensurably to compensate for the reduction in the degree of reinforcement by the SFs so that the overall degree of fiber reinforcement remained the same. The dynamic mechanical properties of the specimens with the different compositions were then determined experimentally and compared.

In order to study the effects of the addition of the fibers on the impact resistance of the SHCC, a reference mixture free of fibers was also tested, and the results were compared with those for the mixtures with the different BF and SF contents. The compositions of the three mixtures with the fibers were 2% BF + 1% SF, 2.5% BF + 0.5% SF, and 3% BF. These mixtures are labeled as BF0SF0 (no fibers), BF2SF1, BF2.5SF0.5, and BF3SF0, respectively. The specific mixing proportions for the SHCC specimens are shown in Table 3.

2.2 Specimen Preparation

First, the aluminate cement, fly ash, silica fume, and the water-reducing agent were mixed in a 20-L planetary cement mortar mixer. Next, water was added to the mixture, which was stirred at 100 rpm for 60 s before being rested for 90 s. The rubber sand on the stirring blade was scrapped into the pot, and the mixture was stirred again at 360 rpm for 120 s. When the fresh mortar had been completely mixed, the BFs and SFs were added slowly into the pot under stirring at 116 rpm for 60 s. The stirring of the mixture was continued at 360 rpm for 60 s before resting for 60 s. The rubber sand on the stirring blade was again scrapped into the pot, and the mixture

**Fig. 1** Tensile test specimen.

was stirred at 360 rpm for another 60 s to complete the specimen preparation process. The fresh mixture was poured into a mold (100 mm × 100 mm × 400 mm) and scratched and then vibrated twice at a high frequency for 60 s. The specimens were cured in a standard curing cabinet for 24 h at a temperature of 20 ± 2 °C and relative humidity of more than 95%. After being demolded, the specimens were placed in a curing chamber at 20 ± 2 °C and a relative humidity of more than 95% for aging. After 28 days, cylindrical specimens with a diameter of 48 mm and thickness of 25 mm were cut from the aged specimens for static and dynamic compressive testing.

For the static tensile test, the specimens were configured into a “dumbbell-like” shape. The length of the tensile section of the specimens was 80 mm, width was 30 mm, and thickness was 12.7 mm, as indicated in Fig. 1 (JC/T2461-2018 2018). The curing procedure for the static tensile test specimens was the same as that for the specimens for the static and dynamic compressive tests.

2.3 Static Mechanical Test

The static compression test was performed by using a 500-kN capacity MATEST (Treviolo, Italy) testing

machine. During the test, an axial compressive force was applied gradually at a constant axial strain rate of $30 \times 10^{-6} \text{ s}^{-1}$. The static tensile test was carried out at a strain rate of $4 \times 10^{-5} \text{ s}^{-1}$ using a SANS universal testing machine. An extensometer was used to measure the deformation of the specimens. Three specimens were tested for each group, and the compressive strength was calculated by averaging the results for the three specimens.

2.4 Dynamic Compressive Test

A 50-mm-diameter Split-Hopkinson pressure bar (SHPB) was used for the dynamic tests. Figure 2 shows a schematic of the SHPB used. The SHPB test system consisted of a striker bar, an input bar, an output bar, a shock absorber, and a data acquisition system. The lengths of the striker, input, and output bar were 397, 2397, and 1391 mm, respectively. These elastic bars were made of high-strength steel with a density of 7850 kg/m^3 and Young's modulus of 210 GPa.

The test specimen was coated with a layer of Vaseline and installed on the SHPB. A rubber sheet with a diameter of 15 mm and thickness of 2 mm was placed on the surface of the input bar as the pulse shaper. During the test, the projectile was driven at pressures of 0.2, 0.35, and 0.56 MPa; the corresponding strain rates were approximately 120, 180, and 230 s^{-1} , respectively. The striker impact velocity ranged from 10 to 19.5 m/s. The speed of the projectile was similar for the same air pressure.

During the test, the impact of the projectile produces a rectangular or trapezoidal compressive pulse, which is transmitted to the incident bar/specimen surface and is reflected partly at each end of the bar. The strain gauges attached to the input and output bars are used to measure the incident, reflected, and transmitted pulses. During the test, the incident pulse, denoted as ε_i , is partly

transmitted to the input bar and the specimens sandwiched between the input and output bars. A portion of the pulse is reflected back to the input bar and is denoted as ε_r , while the remainder is transmitted to output bar and is denoted as ε_t . The responses of the strain gauges are recorded in the form of voltage signals.

The two-wave method was used for processing the SHPB data. It should be mentioned that the tests were based on the following two assumptions: (1) one-dimensional stress wave propagation and (2) stress-strain uniformity. Accordingly, the strain, $\varepsilon_s(t)$, strain rate, $\dot{\varepsilon}_s(t)$, and stress, $\sigma_s(t)$, values of the specimens were derived as follows:

$$\sigma_s(t) = \frac{EA_0}{A_s} \varepsilon_t(t) \tag{1}$$

$$\varepsilon_s(t) = \frac{2C_0}{l_s} \int_0^t [\varepsilon_i(t) - \varepsilon_r(t)] dt \tag{2}$$

$$\dot{\varepsilon}_s(t) = \frac{2C_0}{l_s} [\varepsilon_i(t) - \varepsilon_r(t)] \tag{3}$$

where $\varepsilon_i(t)$ and $\varepsilon_t(t)$ are the incident wave and transmission wave, respectively; $\sigma_s(t)$ is the specimen stress; $\varepsilon_s(t)$ is the specimen strain; $\dot{\varepsilon}_s(t)$ indicates is the specimen strain rate; E , A_0 , and C_0 are the elastic modulus, cross-sectional area of the input bar, and wave velocity of the input bar, respectively; and l_s and A_s are the specimen thickness and cross-sectional area, respectively.

2.5 Dynamic Splitting Test

To elucidate the effects of the artificial stress concentration, the test specimen was placed between the incident rod and the transmission rod using a steel arc block, as

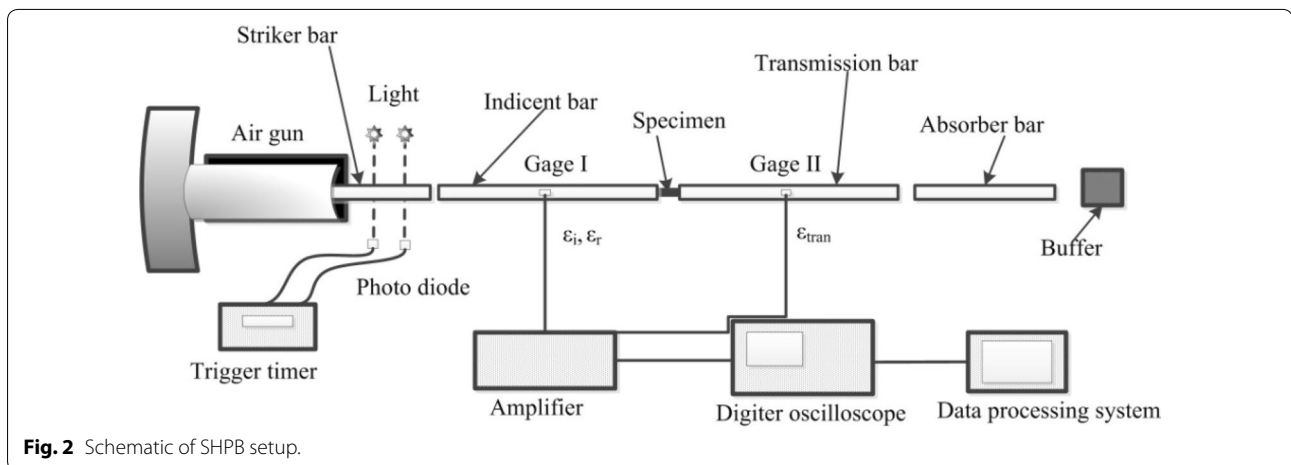


Fig. 2 Schematic of SHPB setup.

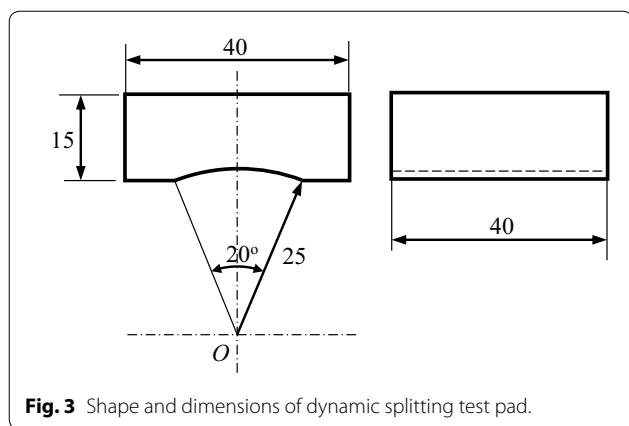


Fig. 3 Shape and dimensions of dynamic splitting test pad.

Table 4 Static compressive and tensile strengths of various specimens.

Specimen ID	BF0SF0	BF3SF0	BF2.5SF0.5	BF2SF1
Compressive strength (MPa)	30.2	34.1	32.6	33.9
Tensile strength (MPa)	3.24	3.87	3.92	4.13

shown in Fig. 3, and all the contact surfaces were coated with Vaseline to reduce friction.

The position of the pressure bar strain gauge was the same as that for the impact compressive tests. The splitting strength, in the context of static elastic mechanics, can be calculated as

$$f_{td} = \frac{2\sigma_t A_0}{\pi h d} \quad (4)$$

where f_{td} is the splitting strength; h is the height of the specimen; d is the diameter of the specimen; σ_t stands for is the maximum stress of the transmitted wave of the pressure bar; and A_0 is the cross-sectional area of the pressure bar.

3 Results and Discussion

3.1 Results of Static Compressive and Tensile Tests

The results of the static tests for the specimens with the different fiber contents are shown in Table 4. The static tensile stress–strain curves are shown in Fig. 4. It can be seen that the specimens with the BF and SF fibers exhibited different strain-hardening behaviors from those of ECCs with PVA, PE, or PP fibers. The static compressive stress–strain curves are shown in Fig. 5. Data analysis indicated that, with the addition of the reinforcing fibers, both the compressive strength and the tensile strength increased significantly. Compared with the compressive strength of specimen BF0SF0, which did not contain any reinforcing fibers, the compressive strengths

of specimens BF3SF0, BF2.5SF0.5, and BF2SF1 were higher by 12.9%, 7.9%, and 12.2%, respectively. Similarly, the respective tensile strengths of specimens BF3SF0, BF2.5SF0.5, and BF2SF1 were higher than that of BF0SF0 by 19.4%, 20.9%, and 27.4%, respectively. During the static tests, specimen BF3SF0 exhibited the highest compressive strength, while specimen BF2SF1 showed the highest tensile strength.

3.2 Results of Dynamic Compressive Tests

3.2.1 Results of Dynamic Compressive Tests and Fracture Patterns

Table 5 shows the dynamic compressive strengths and peak strains of the various samples for four different strain rates. As the strain rate was increased, the dynamic compressive strengths of the specimens with the different fiber contents also increased, while the failure strains decreased initially and then increased. For the same strain rate and a total fiber content of 3%, the dynamic compressive strength of specimen BF2SF1 was higher than those of specimens BF2.5SF0.5 and BF3SF0. Further, as the SF content was increased, the dynamic compressive strength at the same strain rate also increased. It has been reported that, in the case of composites with PVA-SF fibers, the dynamic compressive strength also increases with the SF content (Li et al. 2016). Thus, the results of this study were in keeping with those for a composite with PVA-SF fibers (Li et al. 2016).

The fracture patterns of the specimens under high-strain-rate loading are shown in Fig. 6. Under impact loading, the SHCC specimens fractured primarily because of longitudinal and multidirectional fragmentation. At strain rates of 36–45 s^{-1} , specimen BF0SF0 broke into several large pieces along the loading direction. In contrast, specimens BF3SF0, BF2.5SF0.5, and BF2SF1 showed better performance, as only longitudinal cracks formed along the edges of these specimens, probably owing to the bridging effect of the incorporated fibers. The failure pattern of specimen BF2SF1 was similar to that reported previously for a composite containing only SFs (Hao et al. 2013). Further, for all the strain rates in the range of 50–203 s^{-1} , specimen BF0SF0 underwent fracturing owing to pulverization. However, the degree of damage was reduced after the addition of the reinforcing fibers, since specimens BF3SF0, BF2.5SF0.5, and BF2SF1, which contained the reinforcing fibers, maintained their general integrity at the time of failure, thus confirming the synergistic bridging effect of the BFs and SFs.

3.2.2 Dynamic Stress–Strain Curves

Figure 7 shows the dynamic compressive stress–strain curves of the specimens with the different fiber contents for different strain rates. It can be seen from the figure that the SHCC specimens exhibited an initial linear elastic stage before the peak stress was reached. However,

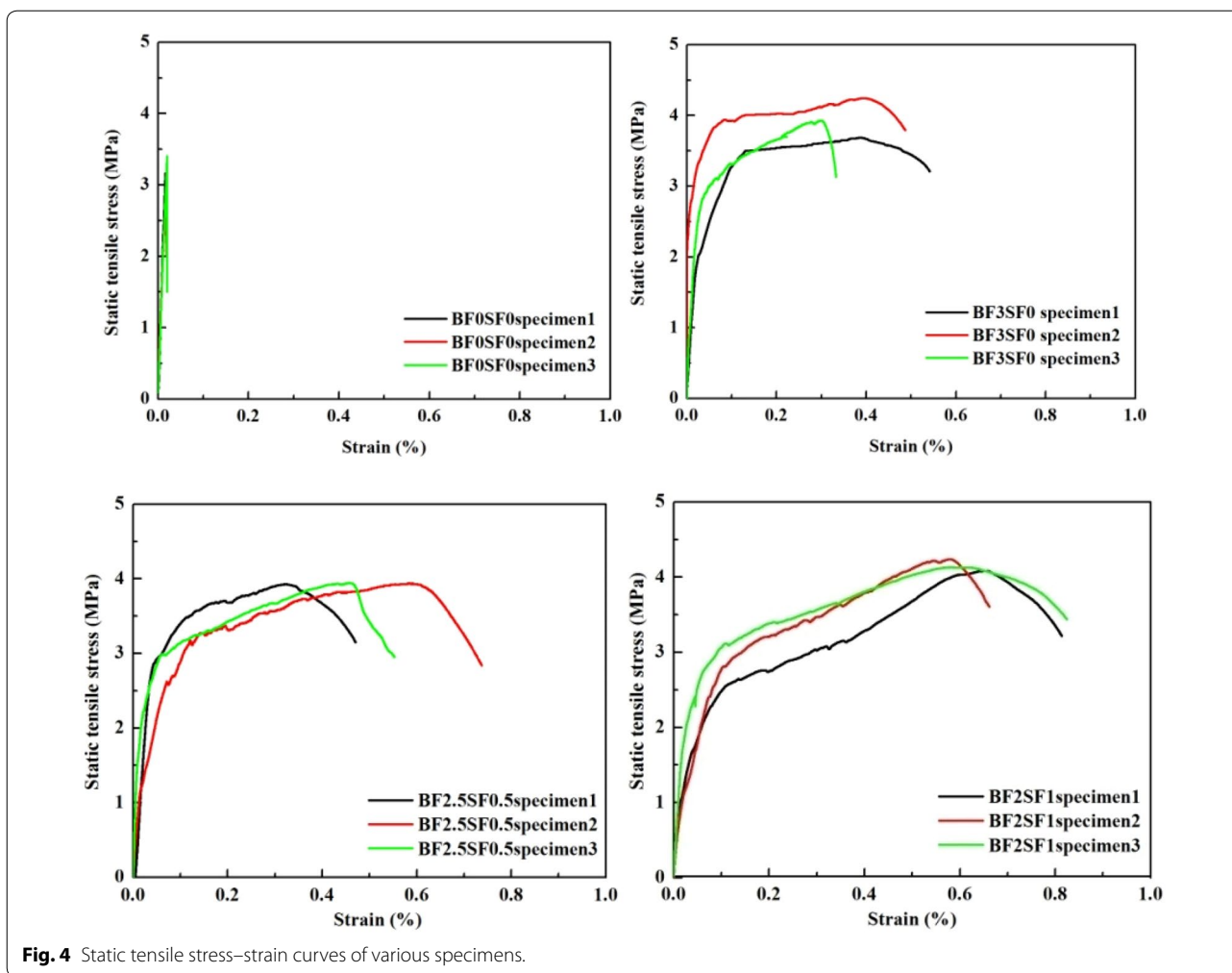


Fig. 4 Static tensile stress–strain curves of various specimens.

once the peak stress had been reached, a downward unloading phase was observed with further increases in the compressive load. All the specimens, namely, those with both BFs and SFs, that with only BFs, that with only SFs, and that consisting only of the cement-based material matrix, were loaded simultaneously. The bridging effect of the fibers was evident in the case of the fiber-reinforced specimens, because as the strain rate was increased, the stress plateau corresponding to the unloading phase in the stress–strain curve was extended. Further, the slope of the decreasing part of the curve also reduced.

As shown in Fig. 7, in the curves for BF3SF0 corresponding to the two lowest strain rates, the peaks were rounder and not very sharp, in contrast to the peaks for the curves corresponding to the other two (higher) strain rates. Thus, it can be concluded that, in the case of the latter two strain rates, the addition of the fibers reduced the integrity of the matrix and resulted in its rapid collapse until the fibers recovered and toughened

after the defects were compacted, resulting in a long unloading section in the curves. The deformation trends of BF3SF0, BF2.5SF0.5, and BF2SF1 at the higher strain rates were similar.

3.2.3 Effect of Strain Rate on Dynamic Increase Factor-Compressive

The dynamic increase factor-compressive (DIF_c) is the ratio of the dynamic compressive strength to the quasi static compressive strength:

$$DIF_c = \frac{f_{dc}}{f_{sc}} \tag{5}$$

where f_{dc} is the dynamic compressive strength and f_{sc} is the static compressive strength.

As per the CEB-FIP Code (2010), the dynamic compressive strength growth factor of ordinary cement concrete can be given by Eq. (6):

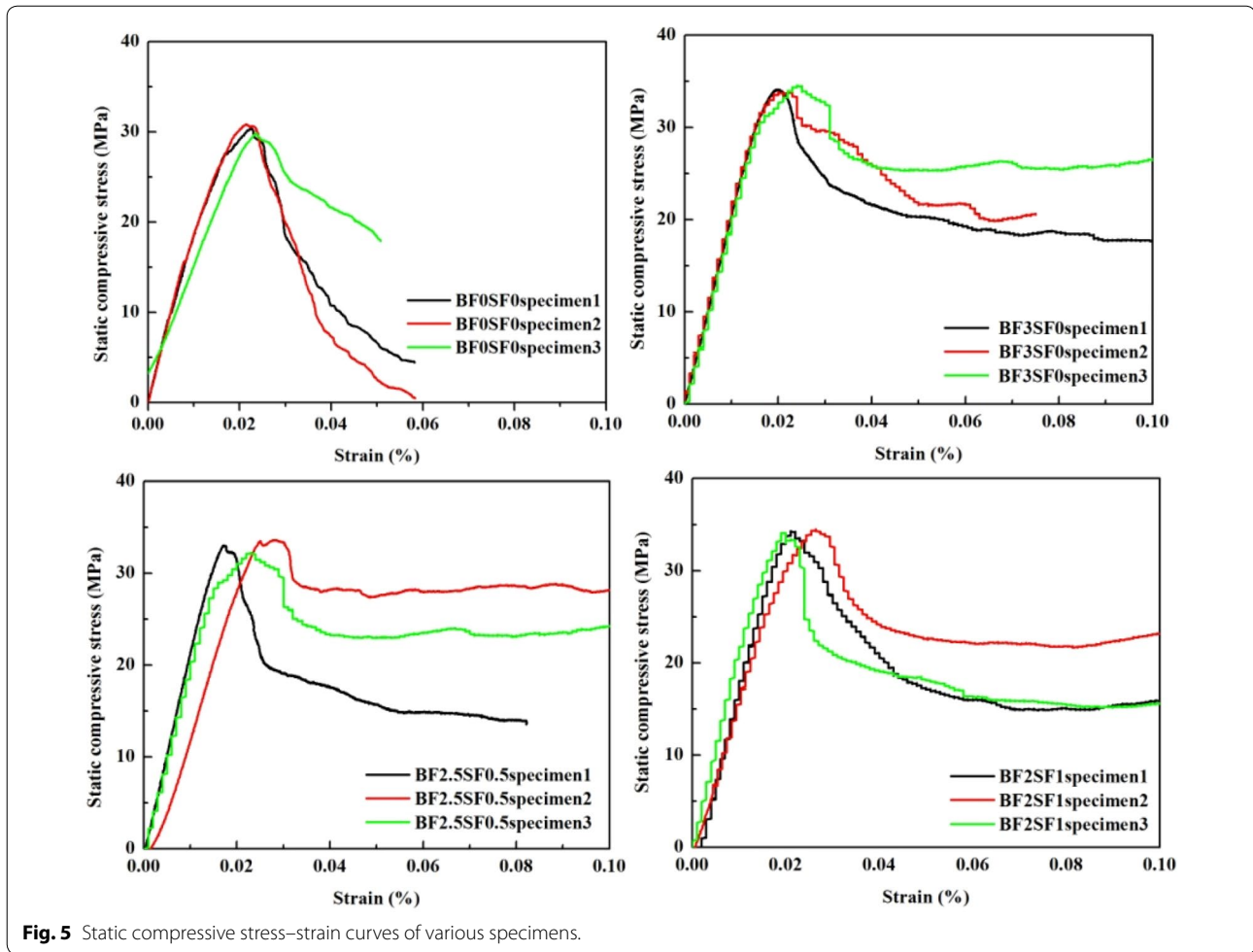


Fig. 5 Static compressive stress–strain curves of various specimens.

$$DIF_c = \begin{cases} (\dot{\epsilon}/\dot{\epsilon}_0)^{0.014} & \dot{\epsilon} \leq 30s^{-1} \\ 0.012(\dot{\epsilon}/\dot{\epsilon}_0)^{\frac{1}{3}} & \dot{\epsilon} > 30s^{-1} \end{cases} \quad (6)$$

where $\dot{\epsilon}_0$ is $3 \times 10^{-5} s^{-1}$. The relationship between DIF_c and the strain rate as determined based on Eq. (6) is shown in Fig. 8.

Based on the ratio of the dynamic peak stress to the quasi static strength, the relationship between DIF_c and the strain rate for the various specimens could be represented using the fitting curves shown in Fig. 8. For strain rates of $35\text{--}203 s^{-1}$, the curves can be approximately as

$$DIF_{BF0SF0} = -0.22378 + 0.93402(\lg\dot{\epsilon}) \quad (7)$$

for $36.1 s^{-1} \leq \dot{\epsilon} \leq 202.3 s^{-1}$

$$DIF_{BF3SF0} = -0.49837 + 1.03467(\lg\dot{\epsilon}) \quad (8)$$

for $44.2 s^{-1} \leq \dot{\epsilon} \leq 172.8 s^{-1}$

$$DIF_{BF2.5SF0.5} = -0.62654 + 1.13344(\lg\dot{\epsilon}) \quad (9)$$

for $43.2 s^{-1} \leq \dot{\epsilon} \leq 190.8 s^{-1}$

$$DIF_{BF2SF1} = -0.5233 + 1.07622(\lg\dot{\epsilon}) \quad (10)$$

for $40.4 s^{-1} \leq \dot{\epsilon} \leq 182.9 s^{-1}$

For cement concrete without any reinforcing fibers, as per the CEB-FIP Code (2010), the dynamic compressive strength increases significantly with increasing strain rate. For the SHCC specimens also, with an increase in the strain rate ($35\text{--}203 s^{-1}$), the dynamic compressive strength increased with the strain rate but with a much smaller slope as compared with that for cement concrete without any reinforcing fibers. Further, with the increase in the fiber content, the trend in the variations in the dynamic compressive strength changed, indicating that the effect of reinforcing fibers on the compressive strength is not always positive. In this study show that both the CEB-FIP fib 2010 equations overestimate the DIF_c values. Finally, the trend in the DIF_c values of the SHCC specimens for the different strains rates were the same as those reported by Chen et al. (2013, 2018) and Wang et al. (2017).

Table 5 Dynamic compressive performances of various samples.

Specimen ID	Strain rate (s^{-1})	Compressive strength (MPa)	Failure strain ($\times 10^{-6}$)
BF0SF0	36.1	36.8	6530
	55.4	43.0	5693
	77.7	46.6	6043
	202.3	58.4	7253
BF3SF0	44.2	39.1	8550
	66.2	47.5	8047
	76.9	53	5320
	172.8	60.7	5967
BF2.5SF0.5	43.2	39.2	7950
	51.8	40.1	6250
	80.8	56.0	7060
	190.8	61.9	6910
BF2SF1	40.4	41.1	6490
	53.1	42.3	5370
	84.0	57.1	6290
	182.9	63.0	7230

3.3 Results of Dynamic Splitting Tests

3.3.1 Dynamic Splitting Test of SHCC Specimens

The splitting tensile strengths of the various fiber-reinforced specimens for the different strain rates are listed in Table 6.

The failure patterns of some of the specimens are shown in Fig. 9. According to Patel et al. (2012), splitting tensile tests cannot accurately determine the direct tensile strength owing to the complex stress fields generated as well as the differences in the orientations of the incorporated fibers. However, the failure modes of the specimens as observed in this study suggested that the SHCC was ductile. This is because, unlike conventional concrete, the fiber-reinforced specimens did not break into pieces after the formation of the first crack, which was probably because of the reinforcing effect of the fibers.

3.3.2 Effect of Strain Rate on Dynamic Splitting Strength

The effective dynamic splitting strengths of each specimen group for the three strain rates were averaged, as shown in Fig. 10. With the increase in the strain rate, the dynamic splitting strengths of the specimens with the different fiber contents exhibited different trends. Generally, as the strain rate was increased, the dynamic splitting strength increased. This was true for all the specimens. Further, for the same strain rate, the dynamic splitting strength of specimen BF2SF1 was greater than those of specimens BF2.5SF0.5, BF3SF0, and BF0SF0. With the addition of the SFs, a higher strain rate resulted in a greater increase in the dynamic tensile strength.

3.3.3 Effect of Strain Rate on Dynamic Increase Factor-Tensile

The dynamic splitting strengths of the specimens with the different fiber contents showed strain-rate sensitivity. To analyze the variations in the case of the SHCC specimens for the different strain rates, the effective splitting tensile strengths of each specimen group for the three strain rates were averaged, as shown in Fig. 11. Analogously to the case for dynamic compression, the dynamic splitting strength enhancement factor, DIF_t , can be defined as

$$DIF_t = \frac{f_{dt}}{f_{st}} \quad (11)$$

where f_{dt} is the dynamic splitting strength and f_{st} is the static splitting strength. For ordinary cement concrete, the dynamic growth factor of the splitting strength can be calculated using Eq. (12), which has been suggested by CEB-FIP Code (2010):

$$DIF_t = \begin{cases} (\dot{\epsilon}/\dot{\epsilon}_0)^{0.018} & \dot{\epsilon} \leq 10s^{-1} \\ 0.0062(\dot{\epsilon}/\dot{\epsilon}_0)^{\frac{1}{3}} & \dot{\epsilon} > 10s^{-1} \end{cases} \quad (12)$$

Through calculations and linear fitting, the relationship between DIF_t and the strain rate could be obtained, as shown in Fig. 11. According to the CEB-FIP Code (2010), the splitting tensile strength of ordinary cement mixtures increases slightly with an increase in the strain rate. In the present study too, with an increase in the strain rate, the splitting tensile strengths of the SHCC specimens (i.e., BF2.5SF0.5, BF2SF, and BF3SF0) increased sharply. Further, the increase in the cases of specimens BF2.5SF0.5 and BF2SF1 was steeper than that for BF3SF0.

Ravichandran and Subhash (1994) compiled a large portion of the available results in the presence of tension. The experimental results obtained in this study were within the range of those previously reported in the literature. For strain rates of 2.8–8.5 s^{-1} , the curves could be approximated as

$$DIF_{t_{BF0SF0}} = 1.53811 + 1.00316(\lg \dot{\epsilon}) \quad (13)$$

for $2.8 s^{-1} \leq \dot{\epsilon} \leq 6.3 s^{-1}$

$$DIF_{t_{BF3SF0}} = 1.40243 + 1.46884(\lg \dot{\epsilon}) \quad (14)$$

for $3.9 s^{-1} \leq \dot{\epsilon} \leq 8.5 s^{-1}$

$$DIF_{t_{BF2.5SF0.5}} = 1.25308 + 1.64636(\lg \dot{\epsilon}) \quad (15)$$

for $4.3 s^{-1} \leq \dot{\epsilon} \leq 8.3 s^{-1}$

$$DIF_{t_{BF2SF1}} = 0.91194 + 2.04797(\lg \dot{\epsilon}) \quad (16)$$

for $4.7s^{-1} \leq \dot{\epsilon} \leq 8.5s^{-1}$.

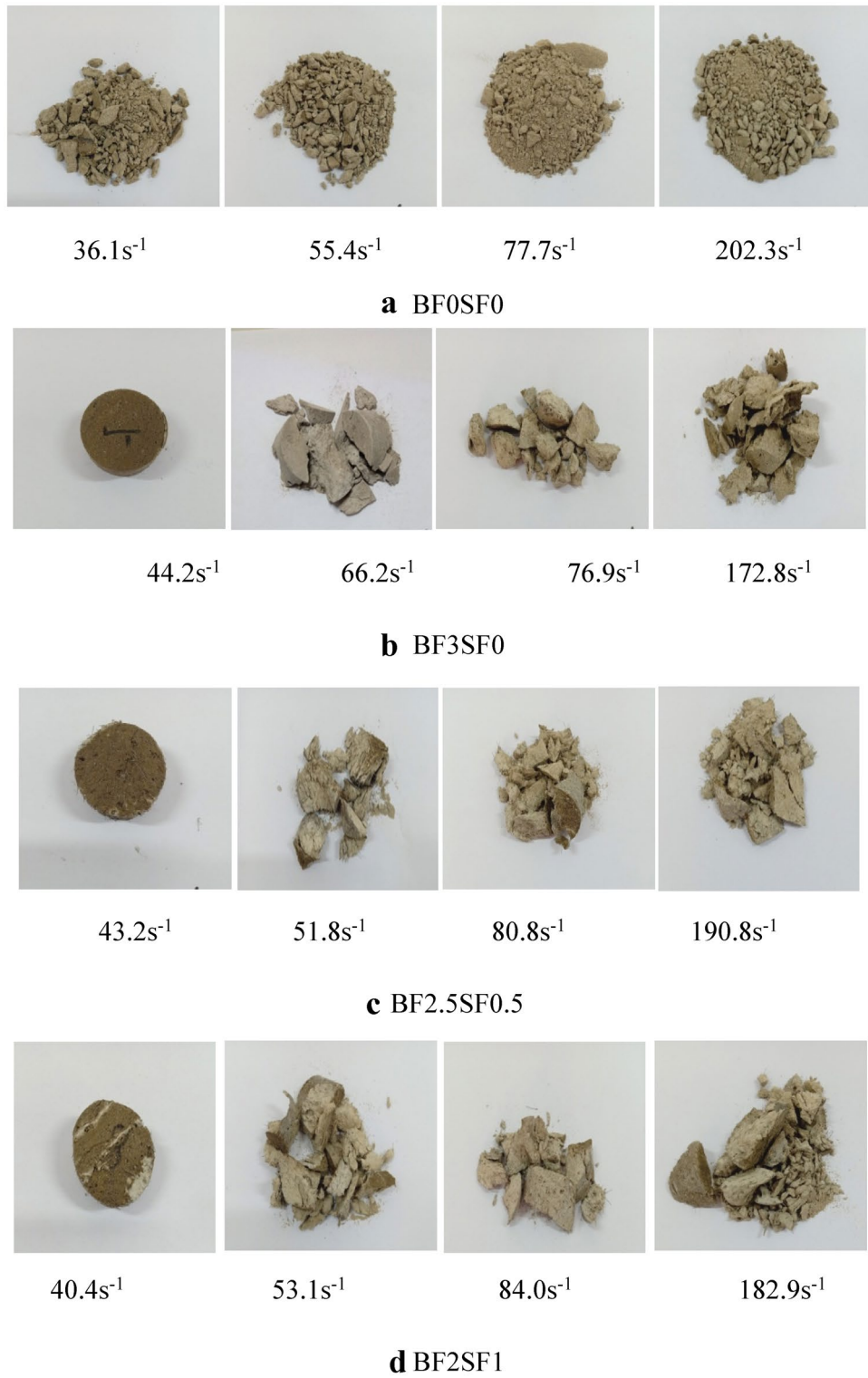


Fig. 6 Fracture patterns of SHCC samples under impact loads corresponding to different strain rates.

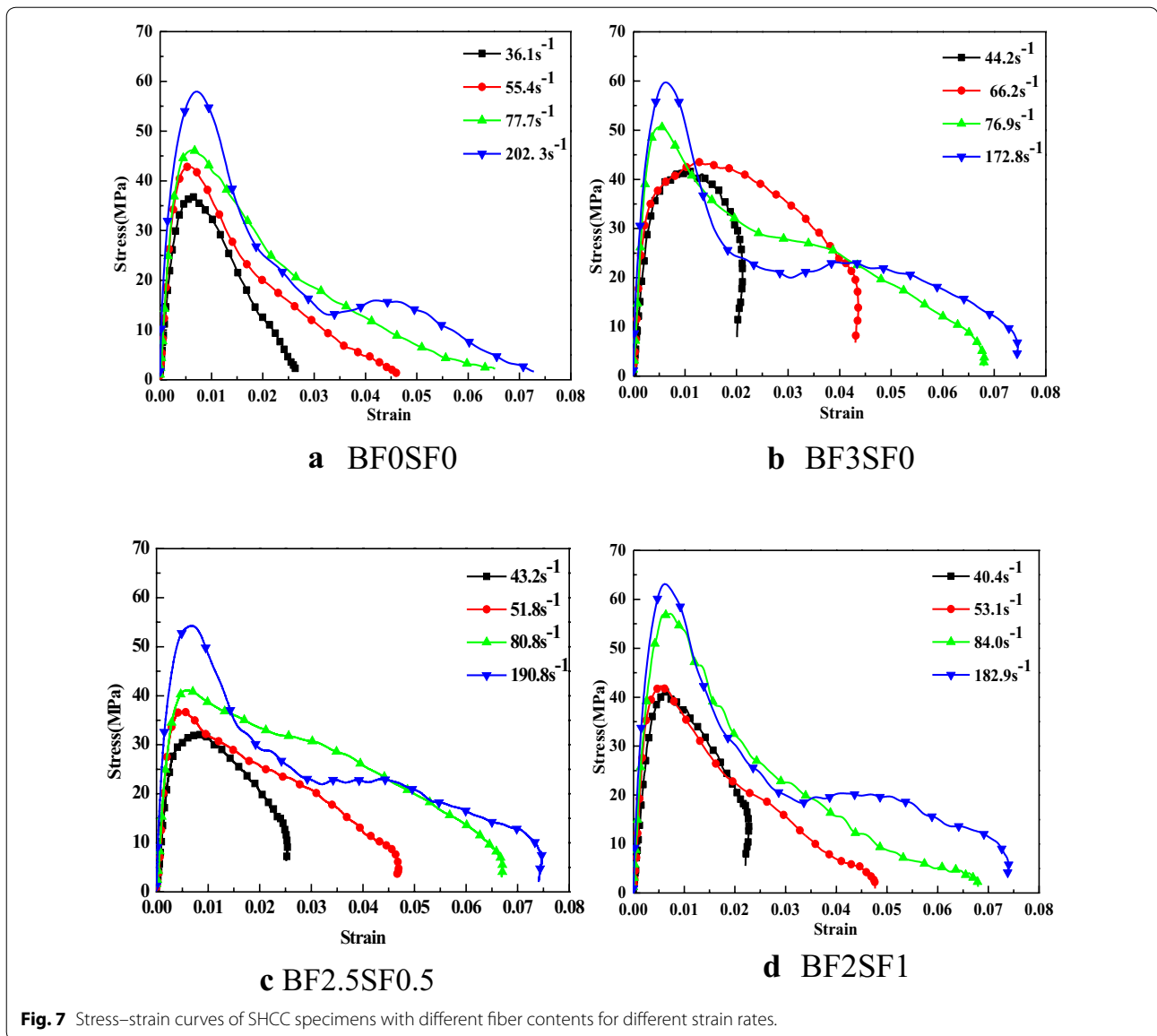


Fig. 7 Stress–strain curves of SHCC specimens with different fiber contents for different strain rates.

3.3.4 Energy Absorption Capacity

The driving factor behind the impact damage incurred by a material is the energy involved. As per the principle of energy conservation, the energy absorbed by the fiber-reinforced SHCC specimens during the SHPB test can be calculated as follows:

$$W_s(t) = W_i(t) - W_r(t) - W_t(t) \tag{17}$$

$$W_i(t) = cEA \int_0^t \varepsilon_i^2 dt \tag{18}$$

$$W_r(t) = cEA \int_0^t \varepsilon_r^2 dt \tag{19}$$

$$W_t(t) = cEA \int_0^t \varepsilon_t^2 dt \tag{20}$$

where $W_i(t)$ is the incident energy, $W_r(t)$ indicates is the reflected energy, $W_t(t)$ represents is the transmitted energy, A is the cross-sectional area of the compression rod, and E and c are the elastic modulus of the compression rod material and the velocity of sound in the material, respectively.

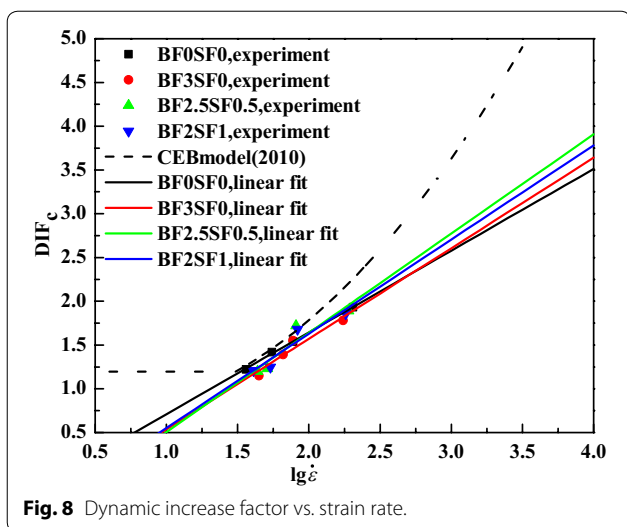


Fig. 8 Dynamic increase factor vs. strain rate.

Table 6 Results of dynamic splitting tests.

Specimen ID	Strain rate (s ⁻¹)	Splitting tensile strength (MPa)
BF0SF0	2.8	6.3
	3.7	7.0
	6.3	7.5
BF3SF0	3.9	8.6
	4.5	9.3
	8.5	10.7
BF2.5SF0.5	4.3	8.9
	5.1	9.6
	8.3	10.8
BF2SF1	4.7	9.5
	6.3	11.2
	8.5	13.3

The maximum dissipative energy of a specimen, $W_{s,max}$, is the value corresponding to splitting test, it can be concluded that most of the energy dissipation corresponded to the tensile damage of the material.

The amount of energy dissipated reflects the energy absorption capacity of the specimen. Using Eq. (13), the dissipated energies for all the specimens subject to dynamic splitting at the different strain rates were calculated. The results are shown in Fig. 12.

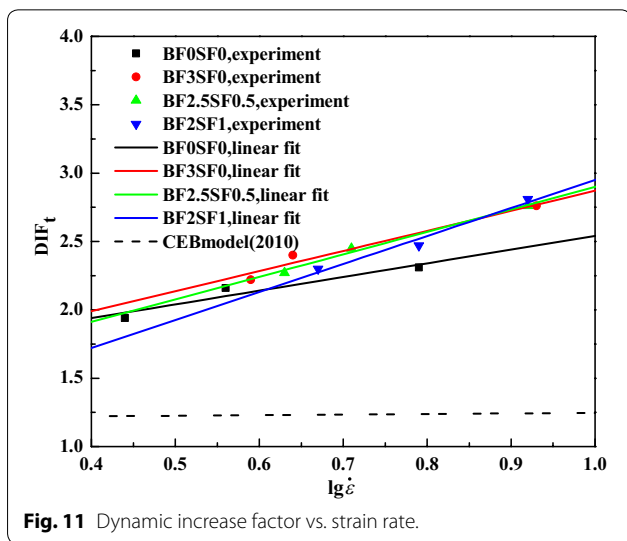
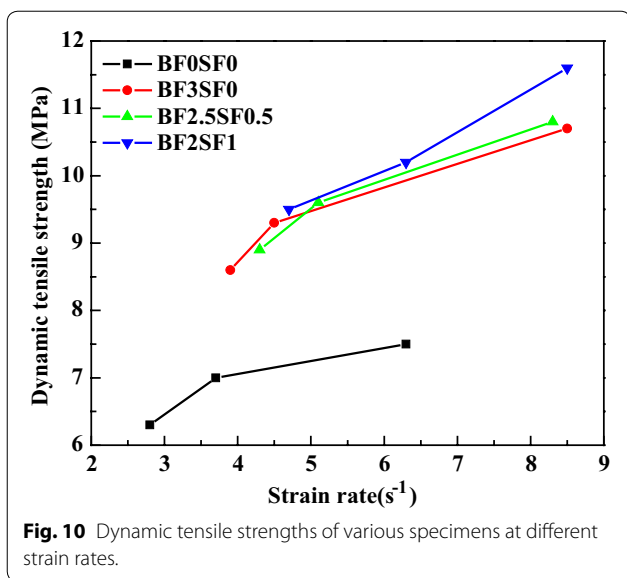
Based on Fig. 11 and Table 7 and the failure modes of the fiber-reinforced SHCC specimens during the dynamic splitting tests, it can be stated that, with an increase in the loading rate, the amount of damage incurred by the specimens also increased. In addition, the amount of energy dissipated during the testing of the SHCC specimens increased with the increase in the strain rate. Thus, the incorporated fibers had a significant effect on the tensile capacity of the SHCC. This phenomenon is consistent with previous findings (Luo et al. 2014; Su et al. 2014). Further, the energy absorption performance of the specimen containing both types of fibers was better than those of the specimens with a single type of fibers. More specifically, at low strain rates, the energy absorption performances of all the specimens were similar, while at high strain rates, the energy absorption performance of the specimen with 1% SFs and 2% BFs was the best.

3.4 Dynamic Mechanical Properties of BF/SF-Reinforced SHCC

In this study, an SHCC was reinforced with fibers of two types, namely, BFs and SFs, in order to improve the fracture characteristics of the cementitious matrix and thus to improve the dynamic mechanical properties of the SHCC. The BFs were smaller in diameter at 14 μm and thus had a larger surface area in contact with the cementitious matrix. In addition, the composition of the BFs was similar to that of the cementitious matrix. This probably helped them form stronger bonds with the matrix. As a result, the BFs exhibited greater interfacial bond strength with the cementitious matrix and helped bridge any small cracks formed. The SFs were 200 μm in diameter and their surfaces were relatively smoother. Consequently, the SFs exhibited relatively low interfacial bond strength with the cementitious matrix and helped bridge larger cracks. In cementitious materials, cracks generate and grow gradually.



Fig. 9 Failure modes of SHCC specimens at lowest strain rate.



Thus, the two-scale reinforcement with the BFs and SFs helped improve the fracture performance of the cementitious matrix and limited crack growth. This trend was consistent with those observed in the case of an ECC prepared using PVA and SFs (Li 2007; Li et al. 2016).

Based on the results of the static compressive and static tensile tests, impact compressive and splitting tests were also performed, and their results were compared with those of the static tests. The compressive and tensile strengths of the SHCC increased with an increase in the

strain rate from a quasi static rate to a moderately high rate. On comparing the results of the impact compressive tests with those of the dynamic splitting tests, it was found that: (1) the dynamic compressive strength and dynamic splitting strength of all the specimens increased with the increase in the strain rate; (2) with the addition of the fibers, the dynamic splitting strength increased more than the dynamic compressive strength, indicating that the bridging effect of the fibers was more pronounced under dynamic tensile loads; (3) the dynamic compressive and splitting strength of specimen BF2SF1 were higher than those of specimens BF3SF0 and BF2.5SF0.5 for the same strain rate; (4) after fiber reinforcement, the compressive DIF did not change significantly with the strain rate, and the slopes of the fitting curves of the various specimens were similar. However, the splitting DIF did change significantly with the strain rate, and the slope of the curve for BF2SF1 was higher than those of the curves for BF3SF0 and BF2.5SF0.5, suggesting that the use of both types of fibers together had a greater effect on the splitting strength than did the use of any one type of fibers.

4 Conclusions

Based on the results of the static and dynamic compressive and splitting tests performed on SHCC specimens containing BFs and SFs in different contents, the following conclusions can be drawn:

1. The dynamic characteristics of the SHCC specimens with the BFs and SFs were extremely sensitive to the strain rate. The dynamic compressive strength, dynamic tensile strength, DIF, and amount of energy absorbed by the SHCC increased with an increase in the strain rate. Further, the dynamic characteristics of specimen BF2SF1 were superior to those of the other specimens.
2. The BFs and SFs had a positive effect on the strain-rate sensitivity of the peak strain, compressive strength, splitting strength, and amount of energy absorbed. For a given fiber content, the use of both BFs and SFs resulted in better mechanical performance than the use of the BFs alone. This indicated that the SFs played the primary role in enhancing the ductility of the cement-based material.
3. The CEB-FIP equation (2010) for estimating the sensitivity rate of ordinary cement concrete is not applicable in the case of SHCCs, as it failed when used to analyze the strain-rate sensitivity of the fabricated

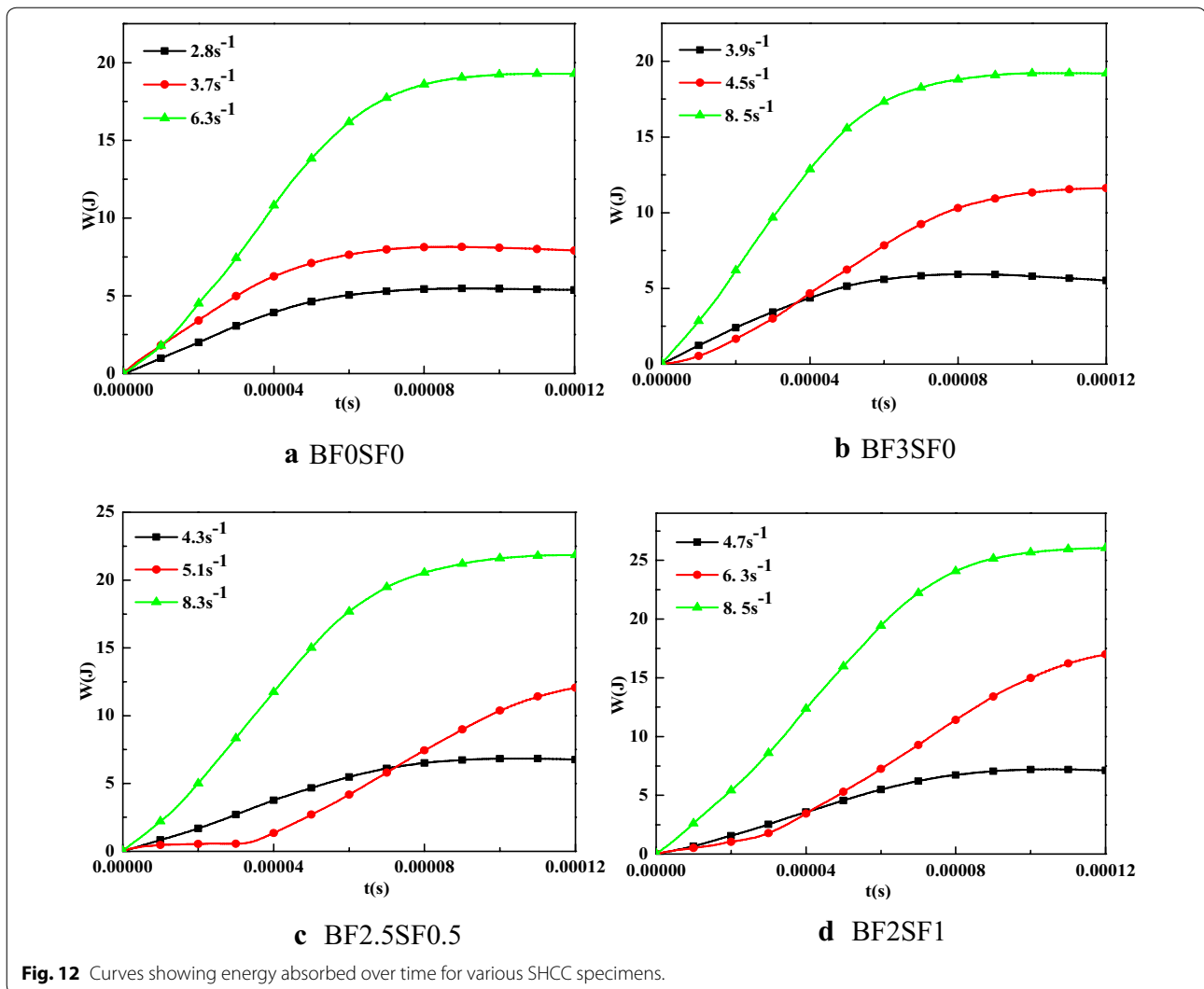


Fig. 12 Curves showing energy absorbed over time for various SHCC specimens.

Table 7 Maximum energy absorbed for various specimens.

Specimen ID	Strain rate (s ⁻¹)	Maximum energy absorbed (J)
BF0SF0	2.8	5.47
	3.7	8.15
	6.3	19.22
BF3SF0	3.9	5.94
	4.5	11.62
	8.5	19.29
BF2.5SF0.5	4.3	6.84
	5.1	12.57
	8.3	21.85
BF2SF1	4.7	7.21
	6.3	17.68
	8.5	26.04

fiber-reinforced SHCC during the dynamic compressive tests for strain rates of 35–203 s⁻¹ as well as during the dynamic splitting tests for strain rates of 2.8–8.5 s⁻¹. Instead, the curve fitting of the experimental results is a more suitable method for studying the strain-rate sensitivity of SHCCs.

Acknowledgements

Not applicable.

Authors' contributions

NZ performed the experiments and analyzed the data. JZ and GW-M provided guidance during the experiments and data analysis and wrote the manuscript. All authors read and approved the final manuscript.

Authors' information

Na Zhang (Ph.D. student) is in School of Civil and Transportation Engineering, Hebei University of Technology, Tianjin 300401, China and lecturer in National Defense Traffic Department, Army Military Transportation University, Tianjin 300161, China, Jian Zhou (Professor) is in School of Civil and Transportation

Engineering, Hebei University of Technology, Tianjin 300401, China, and Guo-wei Ma (Professor) is in School of Civil and Transportation Engineering, Hebei University of Technology, Tianjin 300401, China

Funding

This research was funded by the National Natural Science Foundation of China (NSFC) under Grant numbers 51878238 and 51878241.

Competing interests

The authors declare that they have no competing interests.

Author details

¹ School of Civil and Transportation Engineering, Hebei University of Technology, Tianjin 300401, China. ² National Defense Traffic Department, Army Military Transportation University, Tianjin 300161, China.

Received: 12 January 2020 Accepted: 5 May 2020

Published online: 22 June 2020

References

- Ali, M. A. E. M., Soliman, A. M., & Nehdi, M. L. (2017). Hybrid-fiber reinforced engineered cementitious composite under tensile and impact loading. *Materials and Design*, *117*, 139–149.
- Bhat, P. S., Chang, V., & Li, M. (2014). Effect of elevated temperature on strain-hardening engineered cementitious composites. *Construction and Building Materials*, *69*, 370–380.
- Borhan, T. M. (2012). Properties of glass concrete reinforced with short basalt fiber. *Materials & Design*, *42*, 265–271.
- Branston, J., Das, S., Kenno, S. Y., & Taylor, C. (2016). Mechanical behaviour of basalt fiber reinforced concrete. *Construction and Building Materials*, *124*, 878–886.
- CEB-FIP Model Code. (2010). FIB Model Code for Concrete Structures, Comité Euro-international du Béton–Fédération Internationale de la Précontrainte. Ernst & Sohn
- Chen, D., Feng, L., Fei, Y., Lin, J., Wanhu, F., Jianbing, L. V., et al. (2018). Dynamic compressive and splitting tensile response of unsaturated polyester polymer concrete material at different curing ages. *Construction and Building Materials*, *177*, 477–498.
- Chen, Z., Yang, Y., & Yao, Y. (2013). Quasi-static and dynamic compressive mechanical properties of engineered cementitious composite incorporating ground granulated blast furnace slag. *Materials and Design*, *44*, 500–508.
- Fu, Q., Niu, D., Zhang, J., Huang, D., & Hong, M. (2018). Impact response of concrete reinforced with hybrid basalt-polypropylene fibers. *Powder Technology*, *326*, 411–424.
- GB1596-88. (1988). *Fly ash used in cement and concrete* (in Chinese).
- Hao, H., & Hao, Y. (2013). Dynamic compressive behaviour of spiral steel fiber reinforced concrete in split Hopkinson pressure bar tests. *Construction and Building Materials*, *48*, 521–522.
- JC/T2461-2018. (2018). *Standard test method for the mechanical properties of ductile fiber reinforced cementitious composites* (in Chinese).
- Jiang, C. H., Fan, K., Wu, F., & Chen, D. (2014). Experimental study on the mechanical properties and microstructure of chopped basalt fiber reinforced concrete. *Materials and Design*, *58*, 187–193.
- Kizilkanat, A. B., Kabay, N., Akyüncü, V., Chowdhury, S., & Akça, A. H. (2015). Mechanical properties and fracture behavior of basalt and glass fiber reinforced concrete: an experimental study. *Construction and Building Materials*, *100*, 218–224.
- Lee, J. J., Song, J., & Kim, H. (2014). Chemical stability of basalt fiber in alkaline solution. *Fibers and Polymers*, *15*(11), 2329–2334.
- Li, V. C. (2007). Engineered cementitious composites (ECC)—material, structural, and durability performance. In E. Nawy (Ed.), *Concrete construction engineering handbook* (p. 24). Boca Raton: CRC Press.
- Li, V. C., & Leung, C. K. Y. (1992). Steady state and multiple cracking of short random fiber composites. *ASCE Journal of Engineering Mechanics*, *118*(11), 246–2264.
- Li, Q., Zhao, X., Xu, S., & Gao, X. (2016). Influence of steel fiber on dynamic compressive behavior of hybrid fiber ultra high toughness cementitious composites at different strain rates. *Construction and Building Materials*, *125*, 490–500.
- Lopresto, V., Leone, C., & Lorio, L. D. (2011). Mechanical characterization of basalt fiber reinforced plastic. *Composites Part B Engineering*, *42*(4), 717–723.
- Luo, X., Xu, J., Bai, E., & Li, W. (2014). Study on the effect of basalt fiber on the energy absorption characteristics of porous material. *Construction and Building Materials*, *68*, 384–390.
- Maalej, M., & Li, V. C. (1994). Flexural/tensile strength ratio in engineered cementitious composites. *ASCE Journal of Materials in Civil Engineering*, *6*(4), 513–528.
- Maalej, M., Quek, S. T., & Zhang, J. (2005). Behaviour of hybrid-fiber engineered cementitious composites subjected to dynamic tensile loading and projectile impact. *ASCE Journal of Materials in Civil Engineering*, *17*(2), 143–152.
- Mechtcherine, V., Millon, O., Butle, M., & Thoma, K. (2011). Mechanical behaviour of strain hardening cement-based composites under impact loading. *Cement and Concrete Composites*, *33*(1), 1–11.
- Patel, P. A., Desai, A. K., & Desai, J. A. (2012). Evaluation of engineering properties for polypropylene fibre reinforced concrete. *International Journal of Advanced Engineering Technology*, *3*(1), 42–45.
- Ralegaonkar, R., Gavali, H., Aswath, P., & Abolmaali, S. (2018). Application of chopped basalt fibers in reinforced mortar: a review. *Construction and Building Materials*, *164*, 589–602.
- Ravichandran, G., & Subhash, G. (1994). Critical-appraisal of limiting strain rates for compression testing of ceramics in a Split Hopkinson pressure bar. *Journal of the American Ceramic Society*, *77*(1), 263–267.
- Sim, J. S., Park, C. W., & Moon, D. Y. (2005). Characteristics of basalt fiber as a strengthening material for concrete structures. *Composites Part B Engineering*, *36*(6–7), 504–512.
- Soe, K. T., Zhang, Y. X., & Zhang, L. C. (2013). Impact resistance of hybrid-fiber engineered cementitious composite panels. *Composite Structures*, *104*, 320–330.
- Song, S. (2019). *Research on mechanical properties of basalt fiber reinforced high ductility cement-based composites at room temperature and high temperature*. Tianjin: Hebei University of Technology. (in Chinese).
- Su, H., Xu, J., & Ren, W. (2014). Mechanical properties of ceramic fiber-reinforced concrete under quasi-static and dynamic compression. *Materials and Design*, *57*, 426–434.
- Wang, D., Ju, Y., Shen, H., & Xu, L. (2019). Mechanical properties of high performance concrete reinforced with basalt fiber and polypropylene fiber. *Construction and Building Materials*, *197*, 464–473.
- Wang, S., Le, H. N., Poh, L. H., Quek, S. T., & Zhang, M. H. (2017). Effect of high strain rate on compressive behavior of strain-hardening cement composite in comparison to that of ordinary fiber-reinforced concrete. *Construction and Building Materials*, *136*, 31–43.
- Yang, E. H., Li, V. C. (2005). *Rate dependence in engineered cementitious composites*. In: RILEM workshop on HPPFRCC in structural applications, Honolulu, Hawaii, pp. 83–92.
- Yang, E. H., & Li, V. C. (2012). Tailoring engineered cementitious composites for impact resistance. *Cement and Concrete Research*, *42*(8), 1066–1071.
- Yu, J., Lin, J., Zhang, Z., & Li, V. C. (2015). Mechanical performance of ECC with high-volume fly ash after sub-elevated temperature. *Construction and Building Materials*, *99*, 82–89.
- Zhang, J., Maalej, M., & Quek, S. T. (2007). Performance of hybrid-fiber ECC blast/shelter panels subjected to drop weight impact. *ASCE Journal of Materials in Civil Engineering*, *19*(10), 855–863.

Publisher's Note

Springer Nature remains neutral with regard to jurisdictional claims in published maps and institutional affiliations.